Plane blast wave interaction with an elongated straight and inclined heat-generated inhomogeneity

S. Sembian[1], M. Liverts[1] and N. Apazidis[1],†

[1]Department of Mechanics, KTH - Royal Institute of Technology, SE-100 44, Stockholm, Sweden

The unstable evolution of an elongated elliptically shaped inhomogeneity that is embedded in ambient air and aligned both normal and at an angle to an incident plane blast wave of impact Mach number 2.15 is investigated both experimentally and numerically. The elliptic inhomogeneities and the blast waves are generated using gas heating and exploding wire technique and their interaction is captured optically using shadowgraph method. While two symmetric counter-rotating vortices due to Richtmyer–Meshkov instability are observed for the straight interaction, the formation of a train of vortices similar to Kelvin–Helmholtz instability, introducing asymmetry into the flow field, are observed for an inclined interaction. During the early phase of the interaction process in the straight case, the growth of the counter-rotating vortices (based on the sequence of images obtained from the high-speed camera) and circulation (calculated with the aid of numerical data) are found to be linear in both space and time. Moreover, the normalized circulation is independent of the inhomogeneity density and the ellipse thickness, enabling the formulation of a unique linear fit equation. Conversely, the circulation for an inclined case follows a quadratic function, with each vortex in the train estimated to move with a different velocity directly related to its size at that instant. Two factors influencing the quadratic nature are identified: the reduction in strength of the transmitted shock thereby generating vortices with reduced vorticity, along with the gradual loss of vorticity of the earlier-generated vortices.

Key words: compressible flows, shock waves

---

1. Introduction

Strong coupling of several fluid dynamic phenomena occurs when a shock wave interacts with a density inhomogeneity. This interaction of a pressure discontinuity at an interface between two fluids results in the amplification of disturbances due to baroclinic deposition of vorticity that finally develops into regions of intense mixing, a phenomenon often referred to as the Richtmyer–Meshkov instability (RMI). Secondary instabilities, like the shear-induced Kelvin–Helmholtz instability (KHI), develop at a later time as the interface becomes more distorted. This class of

† Email address for correspondence: nap@mech.kth.se

problems – having diverse applications in the fields of supersonic combustion systems (Scramjet), astrophysical environments of supernovas, supersonic/hypersonic flow control and inertial confinement fusion – has been studied extensively after Richtmyer (1960) first provided the theoretical analysis, and Meshkov (1969) confirmed it experimentally. Zabusky (1999) and Brouillette (2002) gave a comprehensive review on RMI environments and shock accelerated inhomogeneous flows respectively.

A rich literature in the realm of RMI is found for the interaction of a shock wave with an isolated gas bubble, which is a fundamental yet vital configuration for studying shock accelerated inhomogeneous flows. When a shock wave impinges on a bubble, baroclinic vorticity deposition evolves the interface into two counter-rotating vortices, entraining fluid from the surrounding flow and thereby enabling stirring and mixing. Much earlier than all of these events, the impacted incident shock undergoes nonlinear shock effects, like reflection, refraction and diffraction at the gas bubble. Generally, depending on the acoustic impedance of the gas bubble and the surrounding fluid, they are classified as either slow/fast or fast/slow configurations. The same can be classified on the basis of density as heavy/light or light/heavy respectively. A wide variety of investigations covering theoretical, experimental and numerical aspects on light and heavy, cylindrical (two-dimensional) and spherical (three-dimensional) gas bubbles were previously performed. For instance, pioneering work by Markstein (1957) utilized a reactive flame front of an oblong shape to study the shock interaction. Rudinger & Somers (1960) created bubbles using either a spark discharge or fine jet technique to study the effects experimentally and theoretically. Haas & Sturtevant (1987) reported on the shock nonlinear acoustics and evolution of spherical bubbles produced by soap film and two-dimensional (2-D) gas cylinder by a nitrocellulose membrane. Picone & Boris (1988) numerically modelled the experiments conducted by Haas & Sturtevant (1987) and presented an analytical model for calculating circulation, a measure of the net strength of the developed vortices. Another analytical model for circulation was formulated by Yang, Kubota & Zukoski (1994) based on their numerical results. A detailed high-resolution numerical study capturing the nonlinear acoustics and the vortices was performed by Quirk & Karni (1996). By implementing planar laser-induced fluorescence and a seeded round laminar test jet, Jacobs (1992) improved the quality of flow visualization enabling measurement of species concentration and mixing. Layes, Jourdan & Houas (2003, 2005, 2009) utilized a high-speed camera to obtain the evolution from a single run as compared to the single shot images captured previously. Giordano & Burtschell (2006) and Layes & LeMetayer (2007) numerically simulated the experimental results of Layes *et al.* (2003). The effects of a high incident Mach number ($M = 2.95$) were investigated experimentally by Ranjan *et al.* (2005, 2007) and numerically by Niederhaus *et al.* (2007), where they reported a secondary baroclinic source of vorticity. Departure from the single cylinder configuration was initiated by Yang, Kubota & Zukoski (1993) who numerically simulated two and three cylinder interactions in various configurations. Tomkins *et al.* (2003) investigated twin cylinder interactions experimentally which was increased to multiple cylinders by Kumar *et al.* (2007). An in-depth review by Ranjan, Oakley & Bonazza (2011) offers a comprehensive discussion on the shock bubble interaction problem. The common factor in the above stated investigations is the classic circular shape of the bubble whereas studies on different interface shapes are limited. Besides the circular shape, Ray, Samtaney & Zabusky (2000) studied the interaction of a shock wave with a heavy prolate ellipse and provided a heuristic model for calculating interfacial circulation. Bates, Nikiforakis & Holder (2007) studied the evolution of a rectangular block experimentally and numerically.

Large-eddy simulation on a rectangular interface was performed by Wang *et al.* (2010). Zou *et al.* (2010) studied a heavy elliptic cylinder with various aspect ratios, Zhai *et al.* (2014) investigated the interaction with three polygonal interfaces (the square, triangle and diamond) and most recently Georgievskiy, Levin & Sutyrin (2015) numerically studied the shock focusing process in both light and heavy prolate ellipses.

Despite these achievements, the inhomogeneities studied thus far are aligned normal to the incident shock wave, introducing symmetry along the centre axis. The effect of inclining an isolated bubble embedded in the surrounding fluid to the incoming flow field is an area that is unexplored and could potentially open up interesting features, driving future investigations. This paper is focused on exploring the effects of such an inclined isolated bubble introducing asymmetry into the flow field. Geometrically, a circular shape is always symmetric along any axis of incidence of the incident shock and is therefore not suitable for studies pertaining to our problem. The closest shape to a circle covering the complete range of angles between the pressure and density gradients, and still permit inclination, is an ellipse. Here we define the angle of inclination (α) as the angle between the normal to the incident shock and the ellipse major axis. Moreover, we are interested in the dynamic characteristics of the early time development of the vortices, necessitating the need for an elongated ellipse. By early time, we mean the time taken for the fastest shock in the system to reach the downstream interface. However, information on such early time development, even for an uninclined ellipse ($\alpha = 0°$), is very scarce so that a rigorous treatment of it is essential before studying the inclination effects. Therefore the motivation in this paper is twofold: (i) first, to study the early time development of vortices in a straight elongated elliptic configuration ($\alpha = 0°$) and (ii) to extend the knowledge thereby obtained to analyse an inclined elongated elliptic configuration.

Experimentally, generating an elliptic inhomogeneity that can also be inclined is a vital part of the investigation. Inspired by Markstein (1957) and Rudinger & Somers (1960), who utilized heat to create a slow/fast (heavy/light) density inhomogeneity, we implement a new technique based on the principle of 'Joule heating'. This technique, successfully used in our previous work (Sembian, Liverts & Apazidis 2018) to create straight elliptic inhomogeneities ($\alpha = 0°$), is extended in this paper to generate inclined ones. This inhomogeneity is impacted by a plane wave of shock Mach number 2.15 with a blast profile generated by using an exploding wire technique. An existing in-house numerical code solving a full set of 2-D compressible Navier–Stokes equations is used to interpret and analyse the experimentally observed flow features.

Such elongated inhomogeneities are also used in energy deposition problems that are mainly targeted towards flow control and drag reduction in supersonic and hypersonic flight. Energy deposition is a method of controlling the aerodynamic forces and moments through localized regions of thin elongated low density/heated channels (Mirels 1986; Artem'ev *et al.* 1989, 1993; Aleksandrov 1993; Nemchinov *et al.* 1994; Grun *et al.* 1998; Svetsov 2001; Knight, Azarova & Kolesnichenko 2009; Georgievskii, Levin & Sutyrin 2010, 2016; Azarova, Knight & Kolesnichenko 2013), plasma/glow discharge (Klimov *et al.* 1982; Gordeev *et al.* 1996; Ganguly, Bletzinger & Garscadden 1997; Macheret *et al.* 2001; Zudov *et al.* 2003) or jets (Zudov 2010; Tretyakov, Tupikin & Zudov 2012) generated ahead of the vehicle body. A selected survey on drag reduction at high speeds can be found in Knight (2008). Generally, when a shock wave propagates through such channels with a high speed of sound, a thermal precursor shock (a wedge-shaped disturbance) forms as a result of the acceleration of the refracted shock from the incident shock (Mirels 1986; Artem'ev

et al. 1993). This phenomenon was observed much earlier in a classical work by Jahn (1956) due to irregular refraction at the interface between two gas layers. While the influence of magnetic fields on the flow was examined by Aleksandrov (1993), the generation of an intense vortex motion ahead of the vehicle body was investigated by Artem'ev *et al.* (1993). Grun *et al.* (1998) measured the precursor thermal layer with respect to its growth as a function of time. Later Knight *et al.* (2009) and Azarova, Knight & Kolesnichenko (2010), Azarova *et al.* (2013) established three types of vortex related instabilities namely, RMI, KHI and the instability of flat-parallel tangential discontinuity and investigated their influence on drag reduction. Although the elongated heat channels closely resemble the inhomogeneities generated in this work, they were primarily studied from a drag reduction enhancement point of view, with little to no emphasis on the vortex development. Also, the literature on shock interaction with inclined channels is notably meagre apart from the work of Zudov (2010) and Tretyakov *et al.* (2012) who studied an oblique shock interaction with subsonic and supersonic jets where the main focus was on the jet characteristics.

2. Experimental set-up

The experimental set-up and the generation of the inhomogeneity are similar to those in our previous work (Sembian *et al.* 2018). The shock waves are generated by exploding a 0.4 mm diameter copper wire in the test cell consisting of an exploding chamber and a test chamber (figure 1*a*). Both of the chambers are constructed in such a way that a uniform channel of length 360 mm, width 74 mm and height 5 mm runs throughout. The test cell is maintained at an ambient pressure of 1 atm. The wire to be exploded, from here on called the 'exploding wire', is screwed to the electrodes housed in the exploding chamber. The other ends of the electrodes are connected to a 6 μF capacitor charged to 12 kV. Upon discharge, the exploding wire is subjected to very high current, resulting in the generation of a cylindrical blast wave. Since the generated cylindrical wave is confined to a narrow rectangular section, it modifies itself into a plane wave with a blast profile. This plane wave then propagates into the test chamber where a 0.2 mm diameter copper wire (from here on called the 'hot wire' or simply 'wire') is suspended from two 3 mm diameter brass electrodes, one solid (anode) and the other hollow (cathode). Different inclination angles can be obtained by properly positioning the electrodes. The wire is always maintained in a state of tension by passing its other end through a guide cylinder and then connecting it to a freely suspended weight, as shown in figure 1(*b*). The top and bottom wall of the test chamber are made up of Plexiglas plates, providing a maximum field of view of 200 mm in length for visual access. The wire is subjected to a 24 V, 3.6 A current, resulting in heating up of the wire. This in turn heats the air surrounding the wire, producing a density inhomogeneity.

The propagation of the shock wave through the inhomogeneity is captured as shadowgraph images by an optical set-up. Two types of camera are used in capturing the flow structures. A high-speed camera (Shimadzu HPV-X2) set to capture at 0.5 million fps (frames per second) is used for temporal resolution, and a digital still camera (Nikon D90) with 13 MP is utilized for spatial resolution. Images captured using this set-up have a resolution of 0.42 mm pixel^{-1} and 0.07 mm pixel^{-1} respectively. Depending on the camera used, the light source is either a continuous mode argon–ion laser (Spectra-physics BeamLok 2060) or a single pulsed Nd:YAG laser (New wave Orion).

The effective thickness *b* of the inhomogeneity is influenced by the amount of time the wire is subjected to the current. Single-shot shadowgraph images showing the
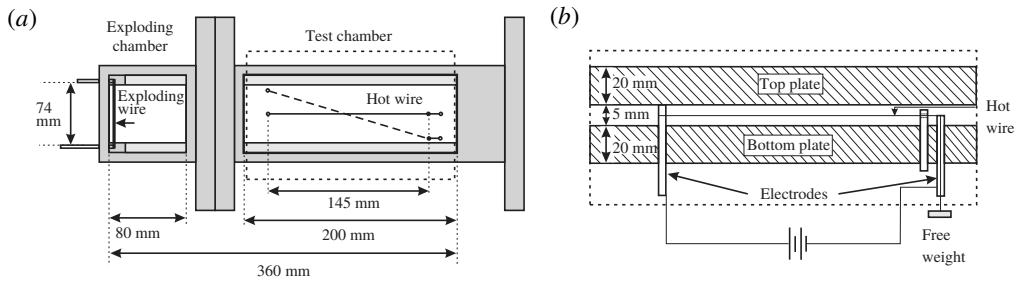
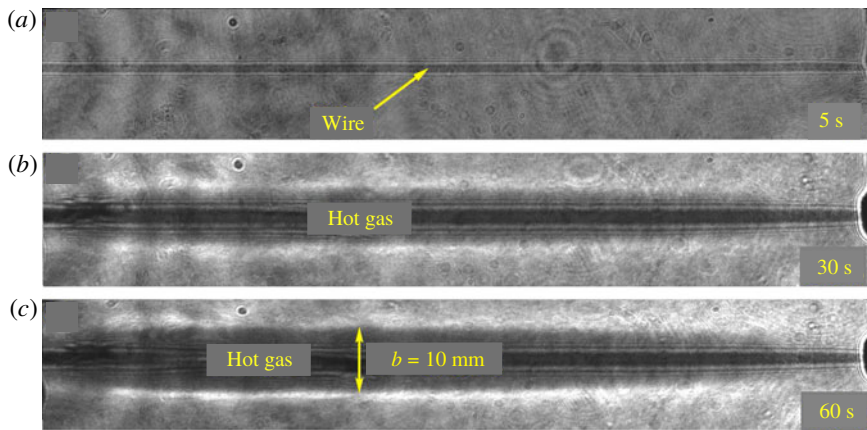FIGURE 1. (*a*) Test unit (top view), (*b*) cut section view of the test chamber (side view).

FIGURE 2. (Colour online) Current supplied time versus heat spread.

effect of the current supply time to the spreading of heat is presented in figure 2. As the wire is suspended in the middle of a thin 5 mm channel, the heat from the wire reaches the Plexiglas plates, making them soft and pliable at the contact region. This affects the optical properties at the surface, making it partially opaque, as depicted by the dark region, indicated by 'Hot gas' in figure 2(*b*). After approximately 60 s, the heat has spread to $b = 10 \pm 2$ mm with an overall shape resembling an ellipse along the inclination axis. Since the heat fills the 5 mm channel (wall to wall) coupled with the subsequent heating of the top and bottom plates, the resulting inhomogeneity is approximated by a D configuration. Although there exists a gradient at the interface with a finite thickness, the distribution of the temperature in the transverse direction can be safely approximated by a step function based on the shape of the transmitted shock. In the presence of large gradients, the transmitted shock will be curved but, as will be shown in § 4, the transmitted shock in our case is very slightly curved, leading to the step function approximation. Also, the observed features were found to be largely unaffected by the temperature gradients, as discussed in Sembian *et al.* (2018).

3. Numerical simulation

The numerical simulations were performed using an existing in-house code solving a full set of 2-D compressible Navier–Stokes equations with air as the test gas.

$$\boldsymbol{U}_t + (\boldsymbol{F}_{a_x} + \boldsymbol{F}_{b_y}) - (\boldsymbol{G}_{a_x} + \boldsymbol{G}_{b_y}) = 0, \tag{3.1}$$

where U represent the vectors of conservative quantities, F_a and F_b the vectors of inviscid flux and G_a and G_b the vectors of viscous flux in the x and y directions respectively.

$$U = \begin{bmatrix} \rho \\ \rho u \\ \rho v \\ \rho E \end{bmatrix}; \quad F_a = \begin{bmatrix} \rho u \\ \rho u^2 + p \\ \rho u v \\ \rho E u + p u \end{bmatrix}; \quad F_b = \begin{bmatrix} \rho v \\ \rho u v \\ \rho v^2 + p \\ \rho E v + p v \end{bmatrix} \quad (3.2a\text{-}c)$$

$$G_a = \begin{bmatrix} 0 \\ \tau_{xx} \\ \tau_{xy} \\ u\tau_{xx} + v\tau_{xy} - q_x \end{bmatrix}; \quad G_b = \begin{bmatrix} 0 \\ \tau_{xy} \\ \tau_{yy} \\ u\tau_{xy} + v\tau_{yy} - q_y \end{bmatrix}, \quad (3.3a,b)$$

where

$$\left. \begin{array}{l} \tau_{xx} = 2\mu u_x - \frac{2}{3}\mu(u_x + v_y); \quad \tau_{yy} = 2\mu v_y - \frac{2}{3}\mu(u_x + v_y); \\ \tau_{xy} = \mu(u_y + v_x); \quad q_x = -\kappa T_x; \quad q_y = -\kappa T_y. \end{array} \right\} \quad (3.4)$$

Here ρ, u, v, p, E, T, denote density, particle velocity components in the x and y directions, pressure, specific total energy and temperature respectively. Dynamic viscosity (μ) (Johnson 2016) and thermal conductivity (κ) for air are temperature dependent and are calculated using the following relations:

$$\left. \begin{array}{l} \mu = \mu_0 \left(\dfrac{T}{T_0} \right)^{1.5} \dfrac{T_0 + 110}{T + 110} \\ \kappa = 1.527\mathrm{e}^{-11}T^3 - 4.8574\mathrm{e}^{-08}T^2 + 1.0184\mathrm{e}^{-04}T - 0.00039333. \end{array} \right\} \quad (3.5)$$

The equation for κ is obtained by curve fitting the data found in Stephan & Laesecke (1985). Other relevant thermodynamic properties of air at normal atmospheric conditions are used. The system of equations are closed by modelling the ideal gas law. Given an interface with normal vector $n = (n_x, n_y)$, U and F can be expressed in the direction of the normal face n as,

$$\begin{bmatrix} \rho \\ \rho q_n \\ \rho q_t \\ \rho E \end{bmatrix} + \begin{bmatrix} \rho q_n \\ \rho q_n^2 + p \\ \rho q_n q_t \\ \rho E q_n + p q_n \end{bmatrix} - G_{x,y} = 0, \quad (3.6)$$

where the normal (q_n) and tangential (q_t) velocities through the interface are given as,

$$\left. \begin{array}{l} q_n = u n_x + v n_y \\ q_t = v n_x - u n_y \end{array} \right\}. \quad (3.7)$$

The equations are solved numerically using a scheme termed AUFSR and proposed by Tchuen *et al.* (2014), which combines the efficiency of artificial upstream flux vector splitting (AUFS) scheme with the accuracy of Roe's solver. The AUFS is a special flux vector splitting (FVS) scheme proposed by Sun & Takayama (2003), that introduces two artificial wave speeds into the flux decomposition to adjust the direction of wave propagation. While it is an accurate and robust technique for resolving entropy waves without the carbuncle problem (MacCormack 2011), it has some shortcomings when resolving shear layers (Kemm 2015). Roe's scheme is a flux difference splitting (FDS) scheme that is known to resolve shear layers

accurately but suffers from the carbuncle problem. The AUFSR overcomes these disadvantages by implementing the artificial wave speed technique with Roe's solver, thereby introducing a certain amount of numerical dissipation to the shear waves. Hence, the AUFSR scheme is not only robust for shock capturing but also accurate for resolving shear layers. The basic idea is to split the flux vector $\boldsymbol{F}$ in (3.6) as,

$$\boldsymbol{F} = (1 - S)\boldsymbol{F}_1 + S\boldsymbol{F}_2, \tag{3.8}$$

where $\boldsymbol{F}_1$ and $\boldsymbol{F}_2$ are the intermediate flux vectors, and $S = s_1/(s_1 - s_2)$, where s_1 and s_2 are the artificial wave speeds. $\boldsymbol{F}_1$ and $\boldsymbol{F}_2$, are calculated from,

$$\boldsymbol{F}_1 = \tfrac{1}{2}(\boldsymbol{P}^L + \boldsymbol{P}^R) + \delta \boldsymbol{U}, \tag{3.9}$$

$$\boldsymbol{F}_2 = \boldsymbol{U}^\zeta (u^\zeta - s_2) + \boldsymbol{P}^\zeta, \quad \zeta = \begin{cases} L & \text{for } s_1 > 0, \\ R & \text{for } s_1 \leqslant 0. \end{cases} \tag{3.10}$$

The artificial viscosity, $\delta \boldsymbol{U}$, is given as

$$\delta \boldsymbol{U} = \frac{1}{2} \left[(q_n^L - s_1)\boldsymbol{U}^L + (q_n^R - s_1)\boldsymbol{U}^R \right] - \frac{1}{2} \sum_{k=1}^{4} |\lambda_k| \eta_k R_k, \tag{3.11}$$

where λ_k, η_k and R_k are the eigenvalues, characteristic variables and eigenvectors calculated using Roe averaged values respectively.

The numerical values of s_1 and s_2 are computed using,

$$\left. \begin{aligned} s_1 &= \bar{q}_n \\ s_2 &= \begin{cases} \min(0, q_n^L - c^L, \bar{q}_n - \bar{c}) & \text{for } s_1 > 0, \\ \max(0, q_n^R + c^R, \bar{q}_n + \bar{c}) & \text{for } s_1 \leqslant 0, \end{cases} \end{aligned} \right\} \tag{3.12}$$

where,

$$\left. \begin{aligned} \bar{q}_n &= \frac{\sqrt{\rho^L}q_n^L + \sqrt{\rho^R}q_n^R}{\sqrt{\rho^L} + \sqrt{\rho^R}} \\ \bar{c} &= \left[(\gamma - 1)\left(\bar{H} - \tfrac{1}{2}\bar{u}^2 \right) \right]^{1/2} \\ \bar{H} &= \frac{\sqrt{\rho^L}H^L + \sqrt{\rho^R}H^R}{\sqrt{\rho^L} + \sqrt{\rho^R}}. \end{aligned} \right\} \tag{3.13}$$

A more detailed description can be found in Tchuen *et al.* (2014).

3.1. *Domain description and initial conditions*

The computational domain of the simulated problem is as shown in figure 3. All boundaries are set with wall boundary conditions. Depending on α, the entire domain was meshed with 2.5–5.5 million cells (unstructured triangle) refined along the axis of inclination. The mesh size varies slowly and smoothly as we go outwards from the axis with the smallest and the largest cell size being 0.025 mm and 0.15 mm respectively. The values of the properties of the flow have stagnated, exhibiting mesh independency. Due to the associated complexities in the problem coupled with the need for large computing resources required to resolve the finer structures, the simulations are performed assuming a 2-D inhomogeneity even for small b values.
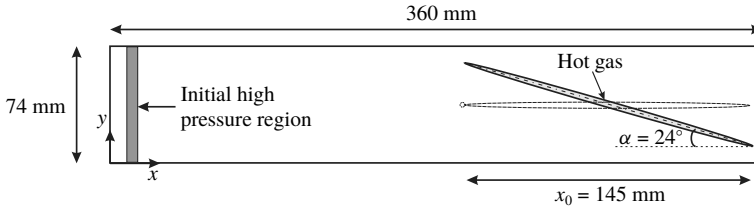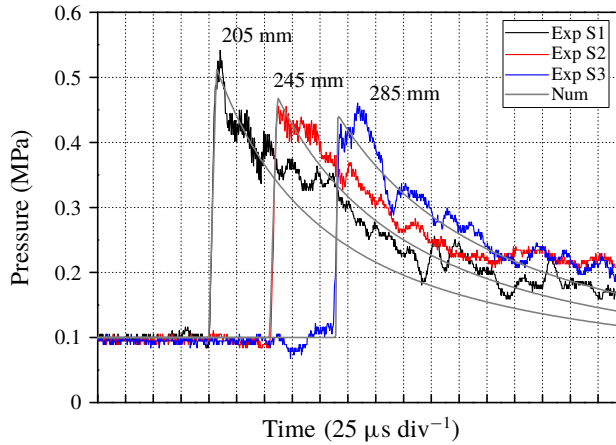
FIGURE 3. Computational domain.

FIGURE 4. (Colour online) Comparison between experimental and numerical pressure trace at three sensor positions: S1 at 205 mm, S2 at 245 mm and S3 at 285 mm from the exploding wire plane.

Although this is an approximation, it will be shown later in §4 that the prediction results are identical to the experiments, justifying the assumption. The numerical analysis can be thought of as an accurate first-order estimate. The experiment was simulated numerically by replacing the exploding wire with a high pressure region with the following initial conditions:

$$(\rho, u, p) = \begin{cases} (140 \text{ kg m}^{-3}, 0 \text{ m s}^{-1}, 15 \text{ MPa}) & \text{for } 1 \text{ mm} \leqslant x \leqslant 3 \text{ mm}, \\ (1.17 \text{ kg m}^{-3}, 0 \text{ m s}^{-1}, 0.1 \text{ MPa}) & \text{for } x \leqslant 1 \text{ mm and } x \geqslant 3 \text{ mm}. \end{cases}$$
(3.14)

The above initial conditions were chosen by trial-and-error method to match the experimental pressure traces obtained from three piezoelectric pressure sensors, S1–S3 (113B24 PCB Piezotronics), flush mounted on the windows at 205 mm, 245 mm and 285 mm from the exploding wire plane, respectively. The uncertainty in determination of the peak pressure amplitude and time of arrival measured from a set of 5 repeatability tests were $\pm 5.5\%$ and $\pm 0.5\%$ respectively. Apart from demonstrating the simulation prediction accuracy, figure 4 also shows the blast wave profile along with its associated shock Mach number at each sensor which were 2.15 ± 0.05, 2.04 ± 0.05 and 1.98 ± 0.05 respectively.

It is important to know the disturbances in the flow due to the 3 mm anode prior to conducting the experiments with the inhomogeneity. In this way, the disturbances can be identified later and neglected from the analysis. As can be seen in figure 5,
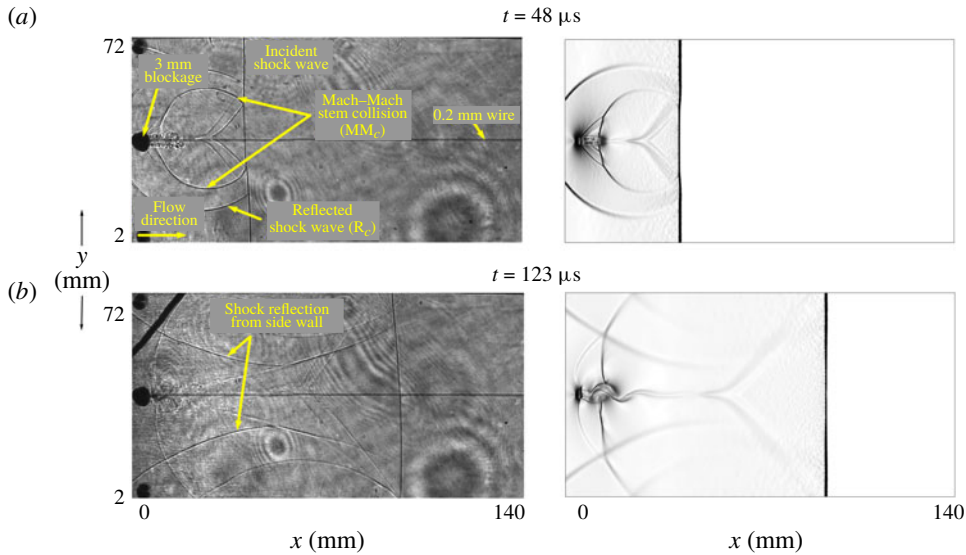
FIGURE 5. (Colour online) Experimental shadowgraph (left) and numerical density gradient (right) images depicting the disturbances due to the anode. The times, (*a*) $t = 48$ µs and (*b*) $t = 123$ µs are relative to the initial shock wave impact at the anode.

the shock diffraction around the anode results in a reflected wave (R_c) and a Mach stem. The collision of the Mach–Mach stem (MM_c) behind the cylinder gives rise to shock patterns, as shown in figure 5(*a*). As it travels downstream, the initial reflected wave get reflected from the side walls forming a 'concave' structure, as in figure 5(*b*). The results of numerical simulation performed with a 3 mm cylinder are shown as a density gradient image beside each shadowgraph image. The magnitude of the density gradient field is calculated as (Quirk & Karni 1996),

$$|\boldsymbol{\nabla}\rho| = \left[\left(\frac{\partial\rho}{\partial x}\right)^2 + \left(\frac{\partial\rho}{\partial y}\right)^2\right]^{1/2}. \tag{3.15}$$

4. Results and discussion

The experiments are conducted for a set of two different inclination angles (α) with each set comprising two b values. The evolution of two straight elliptic inhomogeneities ($\alpha = 0°$) with $b = 3$ mm and 10 mm shocked by an initially plane blast wave of strength Mach 2.15 are as shown in figures 6–8. Figure 6(*a*,*b*) is a single shot shadowgraph image with high spatial resolution while figures 7 and 8 represent images taken with the high-speed camera. With the aid of numerical simulation, the hot gas density (ρ_h) for this case was determined to be 0.5 ± 0.03 kg m^{-3} by a trial-and-error method i.e. by adjusting ρ_h in the simulation until the distance travelled by the incident shock and the transmitted shock matches with the experimental measurement. The corresponding numerical simulation results are shown as density gradient images (*c*,*d*) and vorticity magnitude in figure 6. By juxtaposing experimental and numerical images (figure 6), it can be seen that the simulation captured important structures observed in experiments with sufficient accuracy. As expected, when a shock wave encounters such a medium, it gets reflected and transmitted. Since this is a slow/fast case, the absolute velocity of the transmitted shock wave is higher and
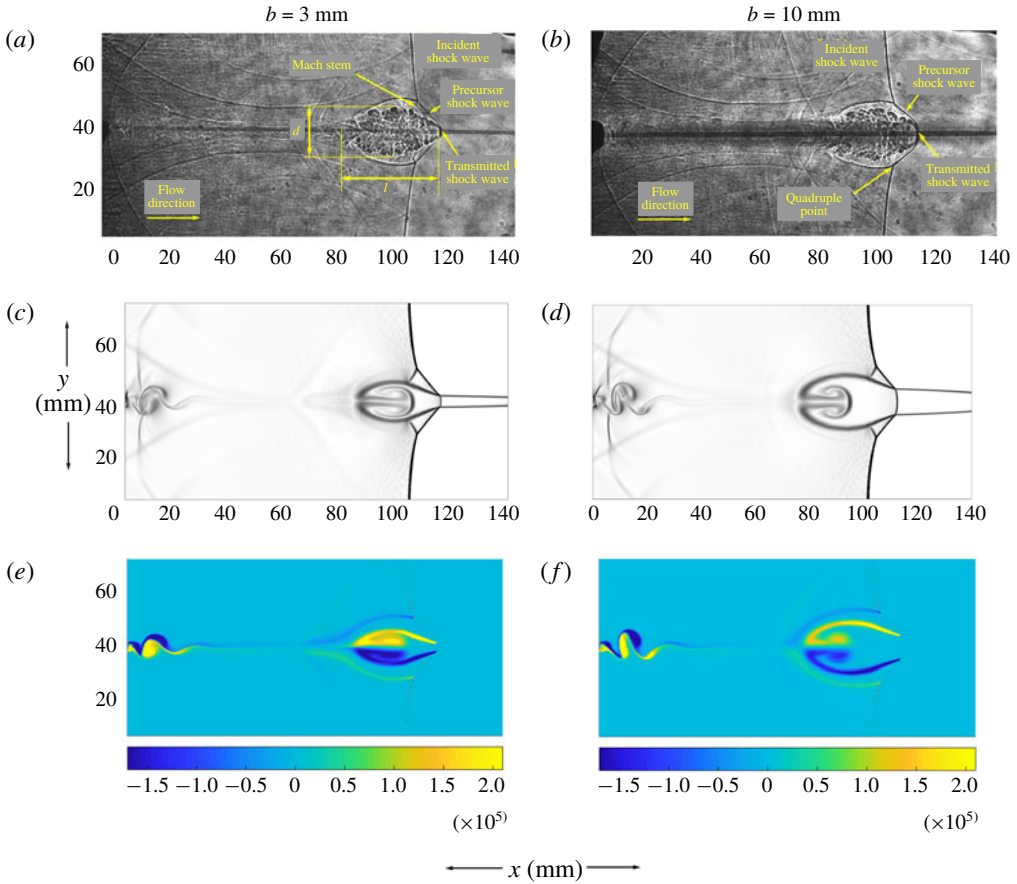
FIGURE 6. (Colour online) Single shot (high spatial resolution) experimental shadowgraph images (a,b) for straight inhomogeneities ($\alpha = 0°$) along with their corresponding numerical density gradient (c,d) and vorticity magnitude (e,f) for the $b = 3$ mm and $b = 10$ mm case.

tends to travel faster than the incident shock. Also, the transmitted shock curvature is very small, justifying the step function approximation for the temperature distribution (Sembian *et al.* 2018). The transmitted shock wave is connected to the incident shock through a precursor shock initiating a quadruple point at its intersection with the Mach stem and reflected shock. The flow field is symmetric along the inclination axis. The transmitted shock propagation speed also varies slightly corresponding to b. For instance, to traverse the 145 mm long inhomogeneity, it takes 180 ± 5 μs and 185 ± 5 μs for $b = 3$ mm and 10 mm respectively. The propagation distance x, defined as the distance travelled by the transmitted shock wave through the inhomogeneity (figure 9a), is measured at an interval of 10 μs and the non-dimensionalized x–t diagram for both thicknesses is plotted in figure 9(b). The propagation distance x is normalized by the overall length of the inhomogeneity ($x_o = 145$ mm) and the time t is normalized with t_o, the time taken to traverse (x_o). The variation is almost linear across both thicknesses and the speed difference is very small compared to the overall propagation time scale.

During this period of shock interaction, vorticity is deposited locally on the interface due to the misalignment between the density and pressure gradients resulting in the
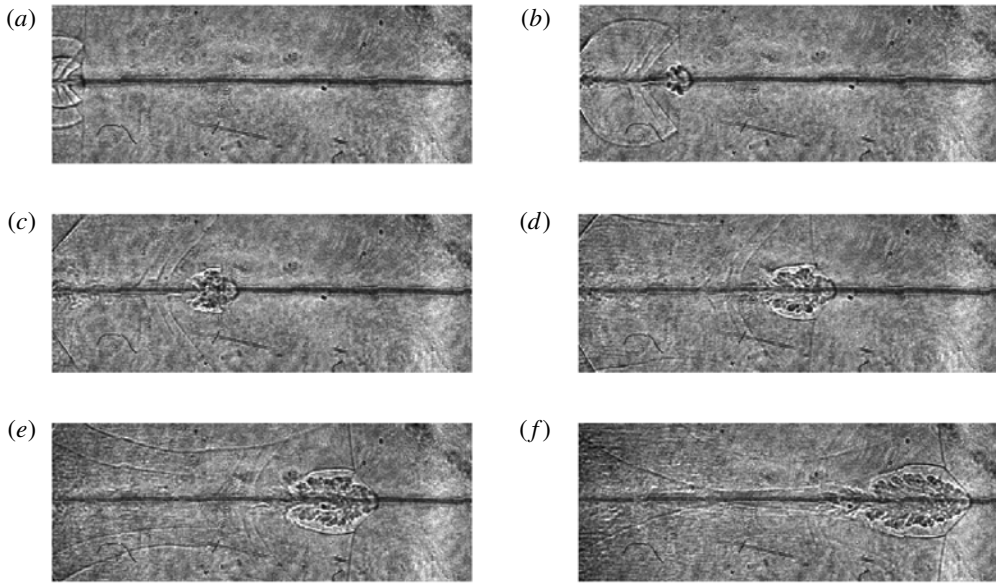
FIGURE 7. Sequence of high-speed experimental images at normalized time $t/t_o = 0.14$, 0.28, 0.42, 0.55, 0.69, 0,83 for $b = 3$ mm case.
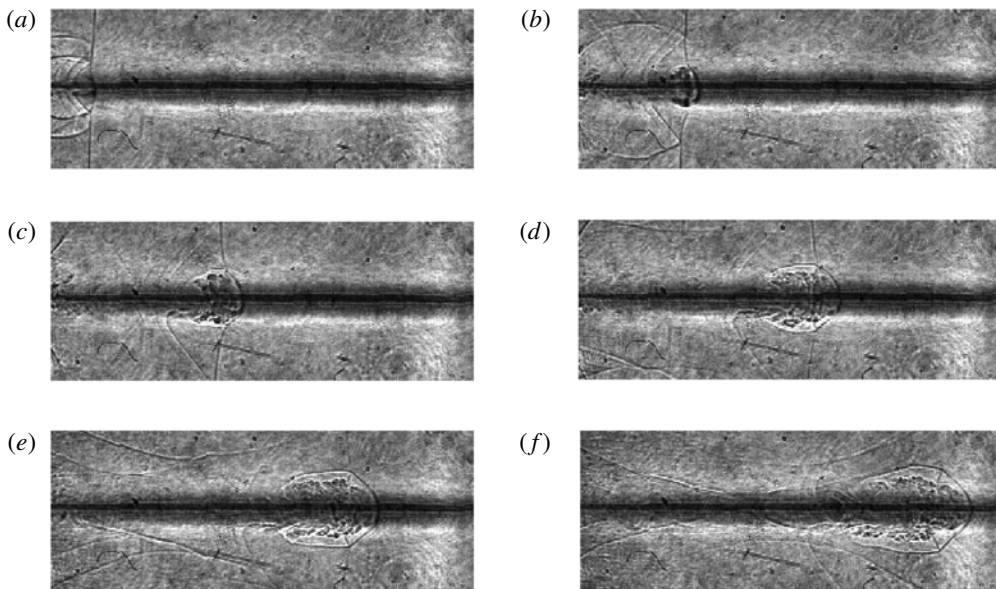

FIGURE 8. Sequence of high-speed experimental images at normalized time $t/t_o = 0.13$, 0.27, 0.41, 0.54, 0.68, 0,81 for $b = 10$ mm case.

formation of two counter-rotating vortices. The sense of rotation of the vortex is clockwise (negative) on the bottom half and counter-clockwise (positive) on the top half, as shown in figure 6(e,f). The vortices are observed experimentally from figures 7(b)–8(b) and grow in both length (l) and width (d) as the shock propagates further into the region. The corresponding vorticity magnitude (top) and density gradient
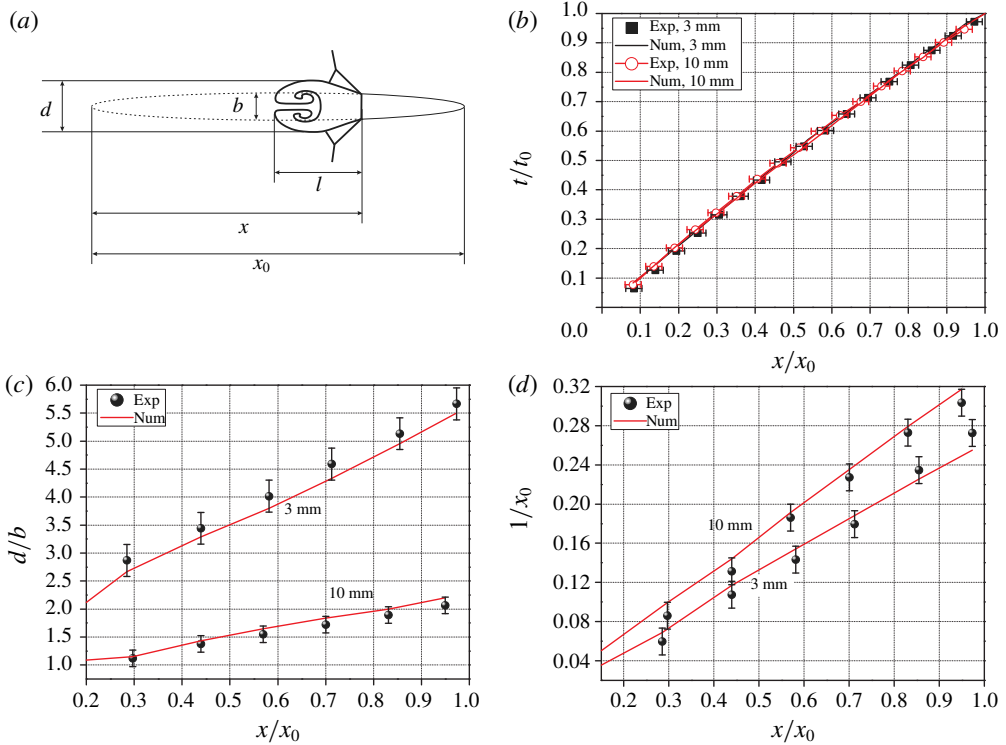
FIGURE 9. (Colour online) (*a*) Schematic drawing illustrating the notations associated with the test configuration; (*b*) normalized propagation distance (x/x_0) as a function of t/t_o; (*c*) normalized width (d/b) and (*d*) normalized length (l/x_0) of the vortices as a function of x/x_0. The corresponding numerical results are also plotted against their experimental values.

(bottom) images are shown in figure 10. The size of the vortices is directly related to the mixing characteristics and therefore is an important parameter to analyse. The width of the vortex is scaled with b, the length with x_o and both are plotted against x/x_o as in figure 9(*c,d*). For $b = 3$ mm, d/b increases and reaches a factor of 5.5 at the downstream interface while it reduces to 2 for $b = 10$ mm. Large factor indicates more fluid being entrained by the vortices from the surrounding fluid. On close observation, it is interesting to note that, irrespective of initial thickness, the location of the quadruple point is fairly similar and the vortices always almost fill up the entire region below them. For example, the quadruple point distance measured from the centre axis in figures 7(*f*)–8(*f*) is ∼10.9 mm and ∼11.4 mm respectively, providing relatively more fluid for entrainment by vortices resulting in large d/b for small b values. Conversely, this also implies minor variations in d across the various thicknesses which is governed by the shock dynamics in the precursor shock region. Similarly, the length (l), which is measured as the distance between the transmitted shock and the downstream edge of the vortex boundary, is also dependent on the precursor shock region and varies linearly with x.

Since this is a slow/fast case, the reflected wave was supposed to be an expansion wave. However, due to the presence of a 3 mm solid cylinder (anode), it was reflected as a shock wave. In order to determine this effect on the shock propagation,
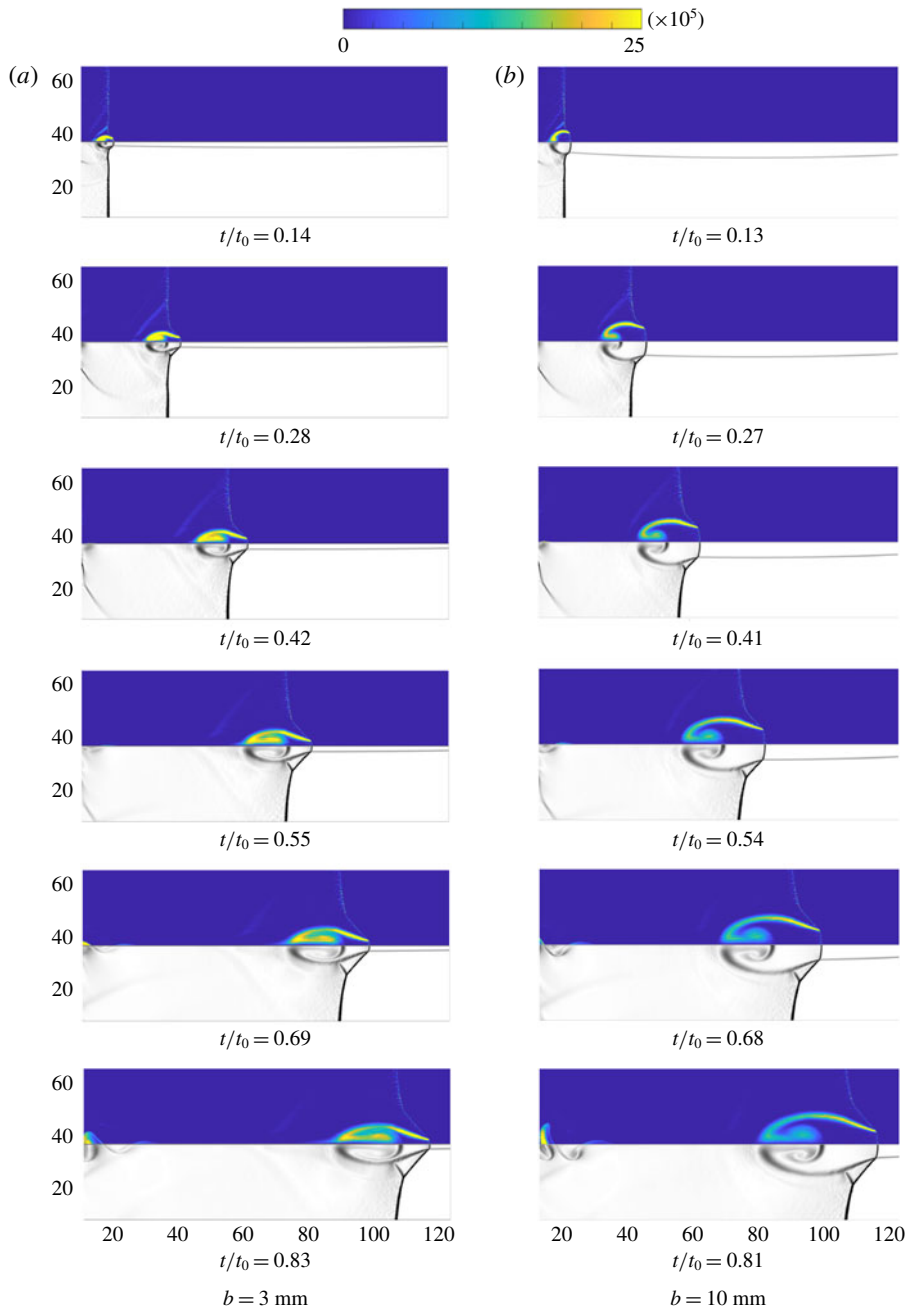
FIGURE 10. (Colour online) Vorticity magnitude (top) and density gradient (bottom) for (a) $b = 3$ mm and (b) $b = 10$ mm straight inhomogeneities. The times t/t_o correspond to their respective high-speed experimental images in figures 7 and 8.

a numerical simulation with no anode is performed and the results are compared in figure 11. The shock structures are observed to be identical in both cases, with no variation in either l or d. Although the anode introduces unwanted shock reflections, this proves that the end results are not affected by it.
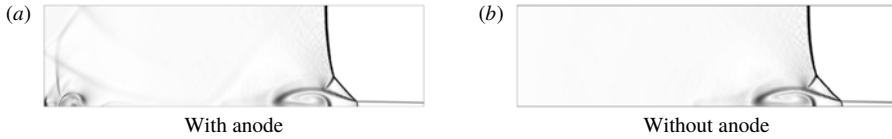
FIGURE 11. Images showing the effects due to the presence of the anode. Apart from the initial shock reflections, the anode does not affect the evolution of the inhomogeneity. Due to symmetry, only the top half is presented.

Circulation Γ, defined as the line integral of velocity around a closed curve, is an important scalar quantity for describing and understanding vortical flows. It quantifies the net strength of the vortices generated by the shock interaction with the inhomogeneity. Several analytical models, like Kelvin's model (Haas & Sturtevant 1987), the Picone and Boris (PB) model (Picone et al. 1984; Picone & Boris 1988), the Yang, Kubota and Zukoski (YKZ) model (Yang et al. 1994), the Samtaney and Zabusky (SZ) model (Samtaney & Zabusky 1994), and the Niederhaus 1-D model (Niederhaus et al. 2007), were formulated to calculate the circulation in shock–bubble interactions. Although the models predict the total circulation (Γ_o) present at the instant of shock passage, the approach and the underlying assumptions made in arriving at the expressions vary. The PB and YKZ models assume that the shape of the bubble and the density ratio do not change significantly during shock passage so that the effects associated with shock refraction are neglected. The SZ model uses the extension of shock polar analysis on planar interfaces by scaling laws to include the refraction effects on circular interfaces. Niederhaus et al. (2007), on the basis of a series of 3-D simulations, formulated a heuristic model reconstructed using 1-D gas dynamic parameters obtained from modelling. However, the common factor in all these models is that they were formulated for a circular interface with a defined radius (R) where the density gradient is normal to the interface as we move radially outward. Ray et al. (2000), extended the SZ model to an elliptic interface but it is applicable only to heavy prolate gaseous ellipses with the major axis along the vertical direction. In the present study, we use a slow/fast elliptic interface – where the density gradient normal to the interface is no longer radial – with the major axis along the horizontal direction, for which models are non-existent. Deriving a formulation for such cases is beyond the scope of this work, and only numerically determined circulation will be presented. Additionally, the models provide the total circulation (Γ_o) only after the fastest shock in the system reaches the downstream interface whereas numerically it can be obtained at every shock instant along x.

Numerically it is calculated following Stokes' theorem that the circulation around a closed curve is equal to the flux of vorticity (ω) through a closed surface S.

$$\Gamma = \oint_S \omega \cdot \mathrm{d}S, \tag{4.1}$$

where

$$\omega = \nabla \times U \tag{4.2}$$

and U is the velocity vector. Figure 12(a) plots the circulation, calculated along the top half of the inhomogeneity, for $b = 3$ mm and 10 mm for every 10 mm transmitted shock passage with the dotted line representing a linear fit. As expected, the circulation value is higher for the 10 mm case at all instants owing to the large initial energy from the hot gas coupled with the relatively small energy dissipation
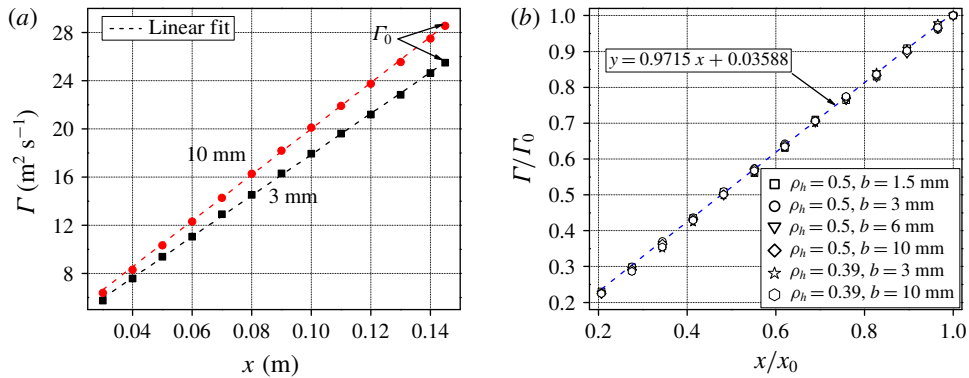
FIGURE 12. (Colour online) (*a*) Numerically computed circulation (Γ) as a function of x for both $b = 3$ and 10 mm case; (*b*) normalized circulation (Γ/Γ_0) for different combinations of b and ρ_h plotted against x/x_0.
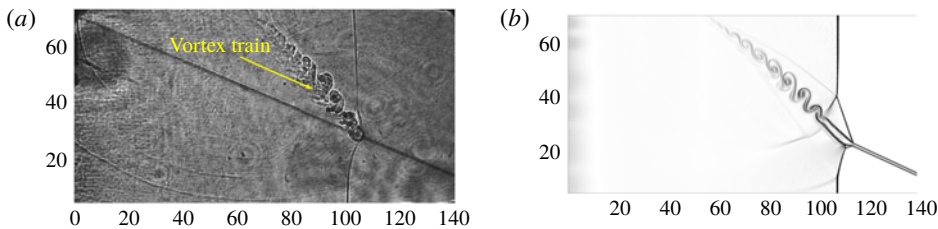

FIGURE 13. (Colour online) Single shot experimental shadowgraph (*a*) and numerical density gradient (*b*) corresponding to $\alpha = 24°$ case for $b = 1.5$ mm depicting the vortex train structure.

through entrainment compared with the 3 mm thickness. Γ at $x = 145$ mm represents the total circulation (Γ_o) corresponding to each b and the normalized Γ/Γ_0 is plotted against x/x_o as in figure 12(*b*). Evidently Γ/Γ_0 falls along the same line represented by one linear fit equation. To examine the effects of thickness and density, simulations were performed for different combinations of b and ρ_h, and the normalized circulation is plotted in figure 12(*b*). It is interesting to note that all data points follow a unique linear fit equation with a measured growth rate of 0.9715 conveniently decoupling the normalized circulation from thickness and density. The Γ_o for all combinations is tabulated in table 1. Since x/x_o varies linearly with t/t_o, the variation of Γ/Γ_0 with t/t_o will also be linear.

The second part of the analysis is done for an inclined inhomogeneity with $\alpha = 24°$. The single shot and high-speed experimental shadowgraph images for $b = 1.5$ mm and 10 mm are as shown in figures 13–15. As with the straight case, the general structures observed here are also similar for both thicknesses. This indicates that the qualitative behaviour is dependant on the inclination angle and not on the thicknesses investigated in this paper. The corresponding numerical density gradient and vorticity magnitude with $\rho_h = 0.39$ for $b = 1.5$ mm are as shown in figure 16. The first and foremost feature observed is the asymmetric flow field along the inclination axis. The transmitted shock rotates itself by α in the clockwise direction and propagates normal to the inclination axis, making it symmetric. However, this introduces an
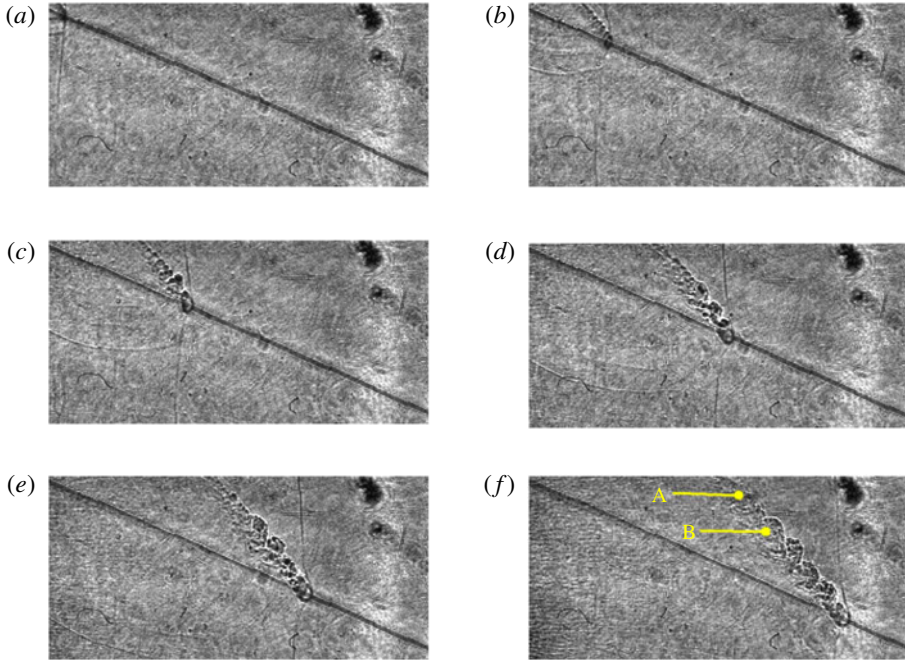
FIGURE 14. (Colour online) Sequence of high-speed experimental images at normalized time $t/t_o = 0.13$, 0.27, 0.41, 0.54, 0.68, 0.81 for $b = 1.5$ mm case.

b (mm)	ρ_h (kg m^{-3})	Γ_o (m^2 s^{-1})
1.5	0.5	22.92
3	0.5	25.34
6	0.5	27.5
10	0.5	28.54
3	0.39	35.48
10	0.39	38.4

TABLE 1. Total circulation (Γ_o) for different combinations of b and ρ_h.

asymmetry to the precursor shock region about the inclination axis. The location of the quadruple point above the axis is far away from the interface, creating an elongated precursor region compared to the bottom. The incident shock is largely unaffected by the inclination as it is seen propagating along the same plane. So the quadruple points can be thought of as acting as a hinge, providing leverage for the transmitted shock rotation by varying the precursor shock length without hindering the incident shock path.

The most striking feature observed is the appearance of a train of vortices that is particularly distinct in figure 13. The vortices are similar in nature to the KHI. During shock passage through the inhomogeneity, the baroclinic mechanism deposits vorticity, initiating an external perturbation at the interface, as seen clearly in figures 14(b) and 15(b). Similar to $\alpha = 0°$, the sense of rotation of vorticity is clockwise (negative) on the bottom interface and counter-clockwise (positive) on the top interface. In addition, the vortices are also embedded in a high velocity region flowing normal to
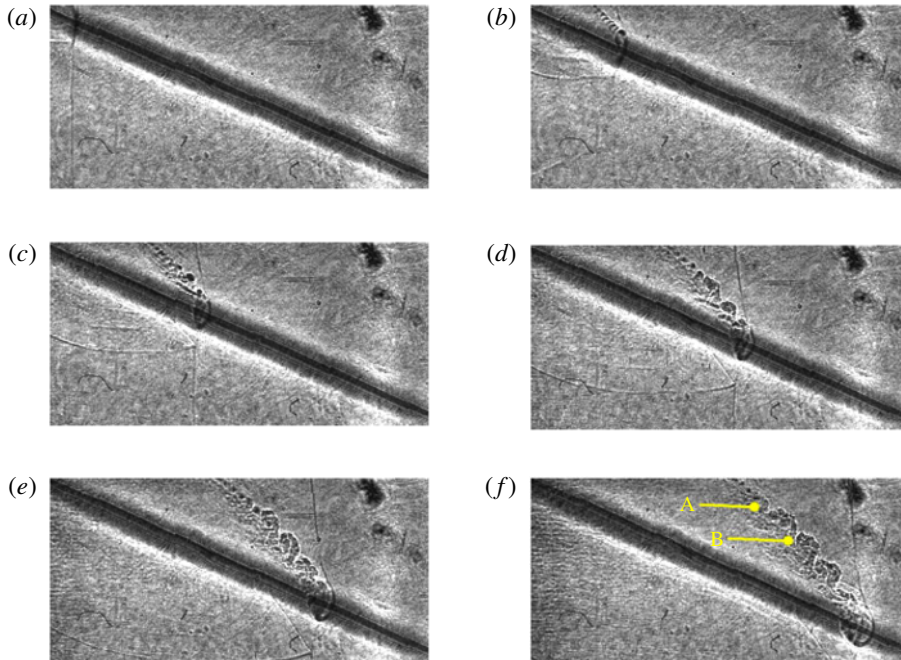
FIGURE 15. (Colour online) Sequence of high-speed experimental images at normalized time $t/t_o = 0.13,\ 0.26,\ 0.39,\ 0.52,\ 0.66,\ 0.79$ for $b = 10$ mm case.

the incident shock which provides additional momentum and sweeps the vortices along its path. During this process, there are effectively two regions of different velocity i.e. the flow due the incident shock and the vortices interacting with each other at an angle. This velocity discontinuity due to the vorticity causes the amplitude of the initial perturbation to grow, resulting in the rolling-up phenomenon of the interface, as seen in figures 14(c–f) and 15(c–f). As the shock traverses the full length, a train of vortices is generated similar to the KHI. As time progresses, the rolled-up vortices continue to grow in size but eventually slow down.

Incidentally, the vortices are also translated normal to the incident shock and can be easily traced to their point of origin. In order to estimate their average translational velocity, two points in the train (marked A and B in figures 14f and 15f) are identified and its path is tracked from the series of images obtained from experiments. The distance travelled from its point of origin (x_{origin}) is fitted against time in figure 17(a) while its corresponding velocity averaged every 10 µs is plotted in figure 17(b) for the $b = 1.5$ mm case. Similar plots for $b = 10$ mm are shown in figure 17(c,d). They are tracked as soon as they are discernible up until t_o. It can been seen that their path follows a quadratic function, consistent with a linear drop in velocity. This is attributed to the energy expenditure associated with the growth of the vortex that entrains more fluid from the surrounding flow. The velocity close to its point of origin (initial velocity) of the generated vortex is dependent on the transmitted shock strength, the source of baroclinicity. But the strength of the transmitted shock gradually reduces as it propagates through the inhomogeneity, resulting in a reduction of the initial velocity of the vortices generated at a later time. This is the reason behind the reduced initial velocity of B compared to A, after which the vortex velocity drops at a constant rate. Also this effectively means that
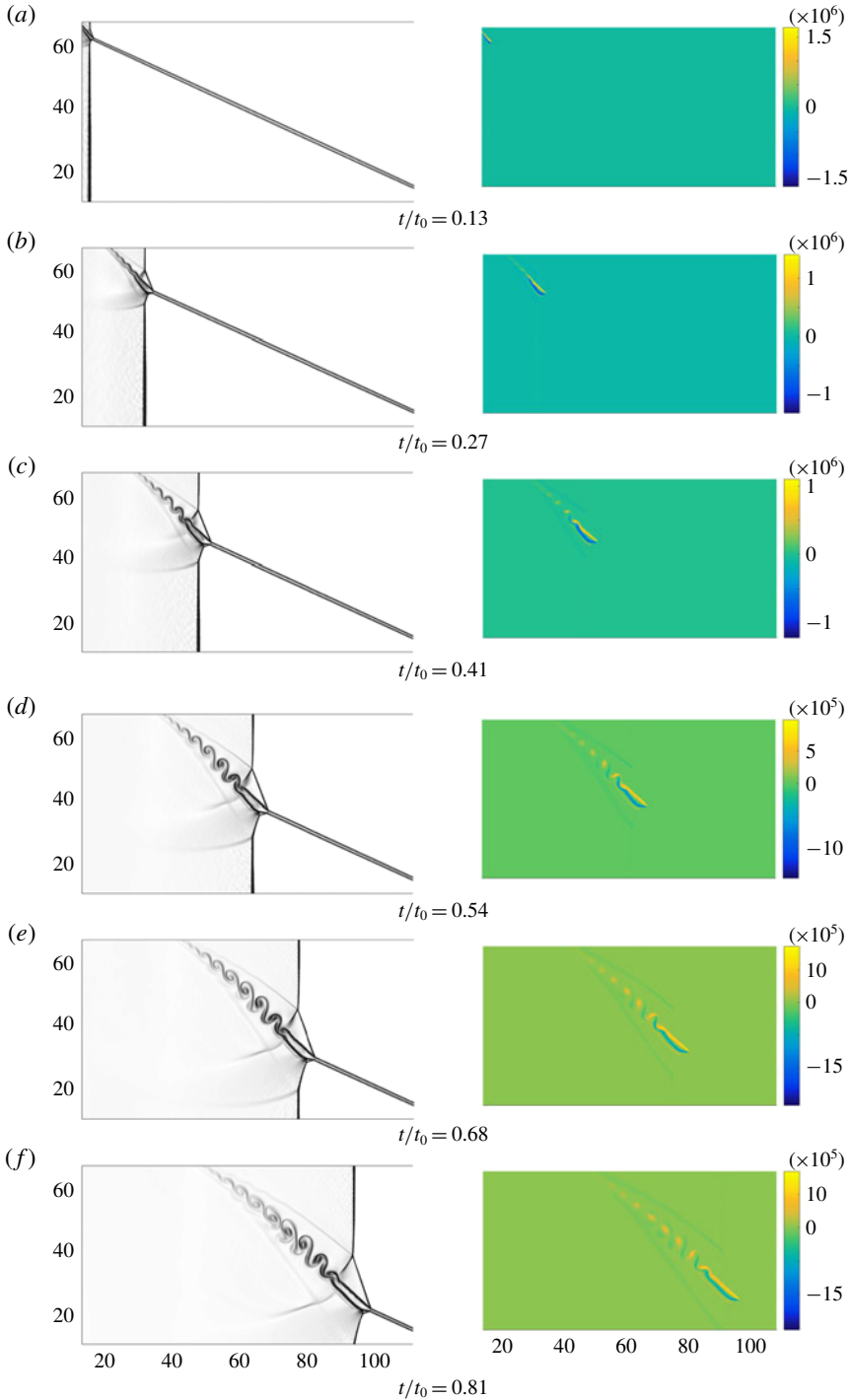
FIGURE 16. (Colour online) Density gradient (left) and vorticity magnitude (right) for $b = 1.5$ mm case. The times t/t_o correspond to their respective high-speed experimental images in figure 14.
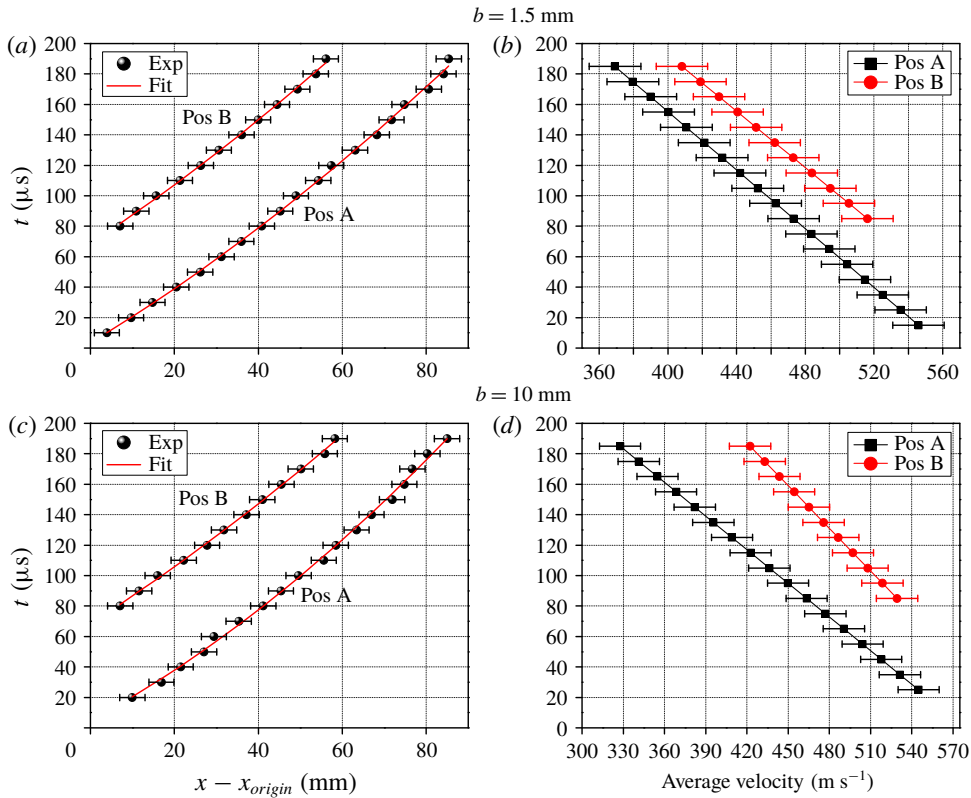
FIGURE 17. (Colour online) (*a*) Distance travelled by points A and B in the vortex train from their point of origin (x_{origin}) and (*b*) their corresponding average velocity plotted against *t* for $b = 1.5$ mm. Similar plots for $b = 10$ mm is shown in (*c*,*d*).

each vortex along the train moves with a different velocity, with the lowest farther away, and the highest close to the transmitted shock. This results in a slight bending of the vortex train, as can be clearly seen in figures 14(*f*)–15(*f*).

The evolution of Γ for $\rho_h = 0.39$ and 0.5 with respect to t/t_o and x/x_o is shown in figure 18(*a*,*b*). As expected, $(\Gamma)_{\rho_h=0.39}$ is larger than $(\Gamma)_{\rho_h=0.5}$ at every point. Also, both the positive (Γ_+) and negative (Γ_-) components of circulation, calculated by integrating only the counter-clockwise and clockwise vorticity respectively, are nearly equal, as can be seen in figure 18(*a*). Unlike the $\alpha = 0°$ case, the variation follows a second-order function. This quadratic nature is influenced by two factors: the reduction in strength of the transmitted shock thereby generating vortices with reduced vorticity, coupled with the gradual loss of vorticity of the earlier-generated vortices. These effects are particularly amplified during the late stage of shock propagation, in this case after $t/t_o, x/x_0 = 0.7$. Γ/Γ_0 for different densities is plotted in figure 18(*c*,*d*). Also included is Γ/Γ_0 from $\alpha = 0°$ for comparison. The normalized circulation also follows a second-order function but is non-unique with the value at each corresponding point larger than that of $(\Gamma/\Gamma_0)_{\alpha=0°}$. It is interesting to note that $(\Gamma/\Gamma_o)_{\rho_h=0.5}$ is slightly larger than $(\Gamma/\Gamma_o)_{\rho_h=0.39}$ despite the opposite trend in Γ variation. This is due to either the lower than expected value of Γ_0 for $\rho_h = 0.5$, or higher than expected value for $\rho_h = 0.39$ for the function to be unique. Therefore the normalized circulation is dependent on ρ_h and a universal fit equation is non-existent.
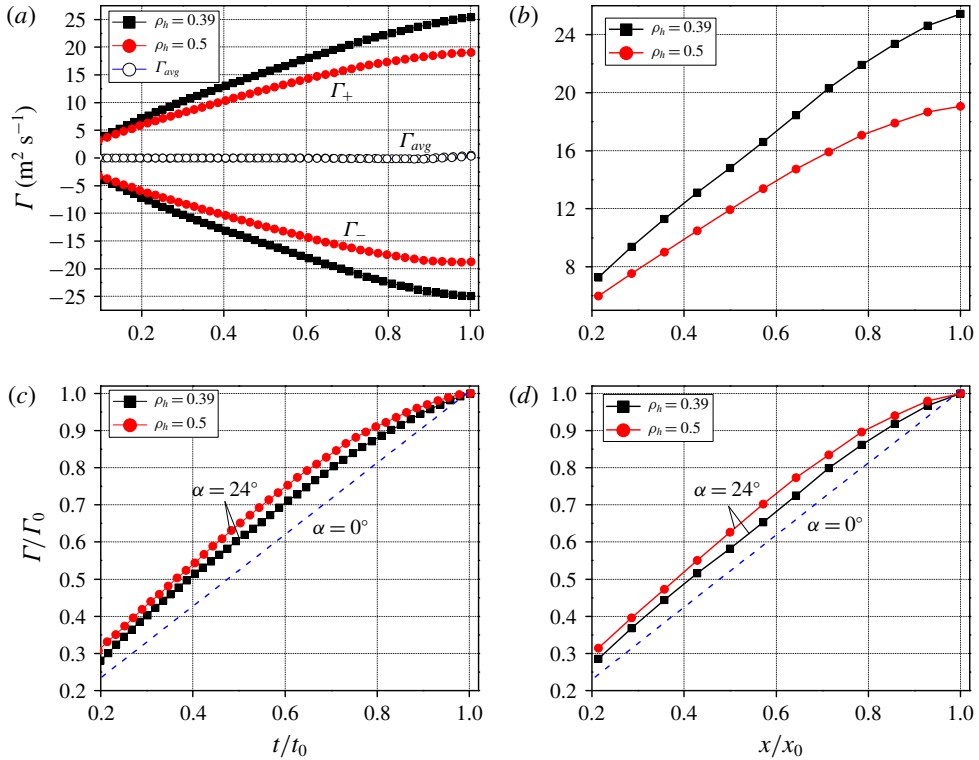
FIGURE 18. (Colour online) (*a*) Numerically computed positive (Γ_+) and negative (Γ_-) circulation for $\rho_h = 0.39$ and 0.5 plotted against t/t_0; due to the symmetric nature of both Γ_+ and Γ_-, only one component is plotted to be consistent with the $\alpha = 0°$ results. (*b*) Circulation (Γ) plotted against x/x_0; normalized circulation (Γ/Γ_0) plotted against (*c*) t/t_0 and (*d*) x/x_0 respectively. Also included in (*c,d*) are the results from $\alpha = 0°$ for comparison.

5. Summary

The results presented here describe the early time interaction of a plane blast wave with an elongated elliptic inhomogeneity, aligned both normal as well as at an angle to the incoming wave. The inhomogeneities were generated on the basis of 'Joule heating' by supplying current to a small conducting wire suspended between two electrodes. This technique provided freedom in the positioning of the electrodes, enabling production of inclined inhomogeneities. The study was performed for two cases: $\alpha = 0°$ and $\alpha = 24°$ with two *b* values. The structures observed in $\alpha = 0°$ were similar to those for a circular bubble, where two counter-rotating vortices were formed due to the RMI. The flow field was symmetric about the centre axis. Since this is an elongated inhomogeneity along the horizontal axis, the baroclinic vorticity deposited along each point at the interface leads to a much faster rolling up of the vortices compared to a circular bubble, enabling early time (time until the transmitted shock reached the downstream interface) study. The variation of the normalized width, length and circulation of the vortices with distance was found to be linear. Also, with the aid of numerical simulation, a unique linear fit equation for normalized circulation was given and it was found to be independent of the

inhomogeneity density and thickness. For the inclined case, the transmitted shock was seen to adjust itself to travel normal to the inclined inhomogeneity with uneven precursor shock regions about the inclination axis. Unlike $\alpha = 0°$, a vortex train similar to the KHI was observed for the $\alpha = 24°$ case. The initial velocity of each individual vortex in the train is dependent on the strength of the transmitted wave and the train was observed to lose its velocity linearly with time as it grew in size. The normalized circulation at each location along x was found to be larger than that for the $\alpha = 0°$ case. Also, it follows a quadratic function influenced by two factors: the reduction in strength of the transmitted shock thereby generating vortices with reduced vorticity and the gradual loss of vorticity of the earlier-generated vortices.

Acknowledgement

REFERENCES

ALEKSANDROV, P. E. 1993 Thermal layer effect in MHD: interaction of a parallel shock with a layer of decreased density. *Shock Waves* **3** (2), 73–78.

ARTEM'EV, V. I., BERGEL'SON, V. I., MEDVEDYUK, S. A., ORLOVA, I. V., NEMCHINOVAND, T. I., RYBAKOV, V. A. & KHAZINS, V. M. 1993 Vortex flows induced by interaction of a shock wave with thin regions of finite length and reduced density. *Fluid Dyn.* **28** (3), 411–414.

ARTEM'EV, V. I., BERGEL'SON, V. I., NEMCHINOV, I. V., ORLOVA, T. I., SMIRNOV, V. A. & KHAZINS, V. M. 1989 Change of regime in supersonic flow past an obstacle preceded by a thin channel of reduced density. *Fluid Dyn.* **24** (5), 779–784.

AZAROVA, O., KNIGHT, D. & KOLESNICHENKO, Y. 2010 Instabilities, vortices and structures characteristics during interaction of microwave filaments with body in supersonic flow. *AIAA Paper* 1004.

AZAROVA, O., KNIGHT, D. & KOLESNICHENKO, Y. 2013 Flow control via instabilities, vortices and steady structures under the action of external microwave energy release. *Proc. Inst. Mech. Engrs* **227** (9), 1498–1515.

BATES, K. R., NIKIFORAKIS, N. & HOLDER, D. 2007 Richtmyer–Meshkov instability induced by the interaction of a shock wave with a rectangular block of SF. *Phys. Fluids* **19**, 036101.

BROUILLETTE, M. 2002 The Richtmyer–Meshkov instability. *Annu. Rev. Fluid Mech.* **34**, 445–468.

GANGULY, B. N., BLETZINGER, P. & GARSCADDEN, A. 1997 Shock wave damping and dispersion in nonequilibrium low pressure argon plasmas. *Phys. Lett.* A **230** (3–4), 218–222.

GEORGIEVSKII, P. Y., LEVIN, V. A. & SUTYRIN, O. G. 2010 Two-dimensional self-similar flows generated by the interaction between a shock and low-density gas regions. *Fluid Dyn.* **45** (2), 281–288.

GEORGIEVSKIY, P. Y., LEVIN, V. A. & SUTYRIN, O. G. 2015 Interaction of a shock with elliptical gas bubbles. *Shock Waves* **25**, 357–369.

GEORGIEVSKII, P. Y., LEVIN, V. A. & SUTYRIN, O. G. 2016 Interaction between a shock wave and a longitudinal low-density gas layer. *Fluid Dyn.* **51** (5), 696–702.

GIORDANO, J. & BURTSCHELL, Y. 2006 Richtmyer–Meshkov instability induced by shock–bubble interaction: numerical and analytical studies with experimental validation. *Phys. Fluids* **18**, 036102.

GORDEEV, V. P., KRASIL'NIKOV, A. V., LAGUTIN, V. I. & OTMENNIKOV, V. N. 1996 Experimental study of the possibility of reducing supersonic drag by employing plasma technology. *Fluid Dyn.* **31** (2), 313–317.

GRUN, J., BURRIS, R., JOYCE, G., SLINKER, S., HUBA, J., EVANS, K., MANKA, C. K., BARTHEL, J. R. & WIEHE, J. W. 1998 Small-scale laboratory measurement and simulation of a thermal precursor shock. *J. Appl. Phys.* **83** (5), 2420–2427.

HAAS, J. F. & STURTEVANT, B. 1987 Interaction of weak shock waves with cylindrical and spherical inhomogeneities. *J. Fluid Mech.* **181**, 41–76.

JACOBS, J. W. 1992 Shock-induced mixing of a light-gas cylinder. *J. Fluid Mech.* **234**, 629–649.

JAHN, R. G. 1956 The refraction of shock waves at a gaseous interface. *J. Fluid Mech.* **1** (5), 457–489.

JOHNSON, R. W. 2016 *Handbook of Fluid Dynamics*. CRC Press.

KEMM, F. 2015 On two deficiencies of the AUFS scheme for Euler flows and possible fixes. *Z. Angew. Math. Mech. J. Appl. Math. Mech.* **95**, 897–910.

KLIMOV, A. I., KOBLOV, A. N., MISHIN, G. I., SEROV, Y. L. & YAVOR, I. P. 1982 Shock wave propagation in a glow discharge. *Sov. Tech. Phys. Lett.* **8** (4), 192–194.

KNIGHT, D. 2008 Survey of aerodynamic drag reduction at high speed by energy deposition. *J. Propul. Power* **24** (6), 1153–1167.

KNIGHT, D., AZAROVA, O. & KOLESNICHENKO, Y. 2009 On details of flow control via characteristics and location of microwave filament during its interaction with supersonic blunt body. In *47th AIAA Aerospace Sciences Meeting including The New Horizons Forum and Aerospace Exposition*, pp. 847–867.

KUMAR, S., VOROBIEFF, P., ORLICZ, G., PALEKAR, A. & TOMKINS, C. 2007 Complex flow morphologies in shock-accelerated gaseous flows. *Physica* D **235**, 21–28.

LAYES, G., JOURDAN, G. & HOUAS, L. 2003 Distortion of a spherical gaseous interface accelerated by a plane shock wave. *Phys. Rev. Lett.* **91**, 174502.

LAYES, G., JOURDAN, G. & HOUAS, L. 2005 Experimental investigation of the shock wave interaction with a spherical gas inhomogeneity. *Phys. Fluids* **17**, 028103.

LAYES, G., JOURDAN, G. & HOUAS, L. 2009 Experimental study on a plane shock wave accelerating a gas bubble. *Phys. Fluids* **21**, 074102.

LAYES, G. & LEMETAYER, O. 2007 Quantitative numerical and experimental studies of the shock accelerated heterogeneous bubbles motion. *Phys. Fluids* **19**, 042105.

MACCORMACK, R. W. 2011 The carbuncle cfd problem. In *Proceedings of the 49th AIAA Aerospace Sciences Meeting*, pp. 381–392.

MACHERET, S. O., IONIKH, Y. Z., CHERNYSHEVA, N. V., YALIN, A. P., MARTINELLI, L. & MILES, R. B. 2001 Shock wave propagation and dispersion in glow discharge plasmas. *Phys. Fluids* **13** (9), 2693–2705.

MARKSTEIN, G. H. 1957 Flow disturbances induced near a slightly wavy contact surface, or flame front, traversed by a shock wave. *J. Aerosp. Sci.* **24**, 238–239.

MESHKOV, E. E. 1969 Instability of the interface of two gases accelerated by a shock wave. *Fluid Dyn.* **4**, 101–104.

MIRELS, H. 1986 Interaction of moving shock with thin stationary thermal layer. *Tech. Rep.*, Aerospace Corp El Segundo Ca Aerophysics Lab.

NEMCHINOV, I. V., ARTEM'EV, V. I., BERGEL'SON, V. I., KHAZINS, V. M., ORLOVA, T. I. & RYBAKOV, V. A. 1994 Rearrangement of the bow shock shape using a hot spike. *Shock Waves* **4** (1), 35–40.

NIEDERHAUS, J. H., GREENOUGH, J. A, OAKLEY, J. G., RANJAN, D., ANDERSON, M. H. & BONAZZA, R. 2007 A computational parameter study for the three-dimensional shock–bubble interaction. *Phys. Rev. Lett.* **98**, 024502.

PICONE, J. M. & BORIS, J. P. 1988 Vorticity generation by shock propagation through bubbles in a gas. *J. Fluid Mech.* **189**, 23–51.

PICONE, J. M., ORAN, E. S., BORIS, J. P. & YOUNG, T. R. JR. 1984 Theory of vorticity generation by shock wave and flame interactions. *Tech. Rep.*, Naval Research Lab Washington DC.

QUIRK, J. J. & KARNI, S. 1996 On the dynamics of a shock–bubble interaction. *J. Fluid Mech.* **318**, 129–163.

RANJAN, D., ANDERSON, M., OAKLEY, J. & BONAZZA, R. 2005 Experimental investigation of a strongly shocked gas bubble. *Phy. Rev. Lett.* **94**, 184507.

RANJAN, D., NIEDERHAUS, J., MOTL, B., ANDERSON, M., OAKLEY, J. & BONAZZA, R. 2007 Experimental investigation of primary and secondary features in high-Mach number shock–bubble interaction. *Phy. Rev. Lett.* **98**, 024502.

RANJAN, D., OAKLEY, J. & BONAZZA, R. 2011 Shock–bubble interactions. *Annu. Rev. Fluid Mech.* **43**, 117–140.

RAY, J., SAMTANEY, R. & ZABUSKY, N. J. 2000 Shock interactions with heavy gaseous elliptic cylinders: two leeward-side shock competition modes and a heuristic model for interfacial circulation deposition at early times. *Phys. Fluids* **12**, 707–716.

RICHTMYER, R. D. 1960 Taylor instability in shock acceleration of compressible fluids. *Commun. Pure Appl. Maths* **13**, 297–319.

RUDINGER, G. & SOMERS, L. M. 1960 Behaviour of small regions of different gases carried in accelerated gas flows. *J. Fluid Mech.* **7**, 161–176.

SAMTANEY, R. & ZABUSKY, N. J. 1994 Circulation deposition on shock-accelerated planar and curved density-stratified interfaces: models and scaling laws. *J. Fluid Mech.* **269**, 45–78.

SEMBIAN, S., LIVERTS, M. & APAZIDIS, N. 2018 Plane blast wave propagation in air with a transverse thermal inhomogeneity. *Eur. J. Mech. (B/Fluids)* **67**, 220–230.

STEPHAN, K. & LAESECKE, A. 1985 The thermal conductivity of fluid air. *J. Phys. Chem. Ref. Data* **14**, 227–234.

SUN, M. & TAKAYAMA, K. 2003 An artificially upstream flux vector splitting scheme for the Euler equations. *J. Comput. Phys.* **189**, 305–329.

SVETSOV, V. 2001 Vortical regime of the flow behind the bow shock wave. *Shock Waves* **11** (3), 229–244.

TCHUEN, G., FOGANG, F., BURTSCHELL, Y. & WOAFO, P. 2014 A hybrid numerical method and its application to inviscid compressible flow problems. *Comput. Phys. Commun.* **185**, 479–488.

TOMKINS, C., PRESTRIDGE, K., RIGHTLEY, P., MARR-LYON, M., VOROBIEFF, P. & BENJAMIN, R. 2003 A quantitative study of the interaction of two Richtmyer–Meshkov-unstable gas cylinders. *Phys. Fluids* **15**, 986–1004.

TRETYAKOV, P., TUPIKIN, A. & ZUDOV, V. 2012 Interaction of a shock wave with a contact discontinuity for local heat release in a flow. In *28th International Symposium on Shock Waves*, pp. 887–892. Springer.

WANG, T., BAI, J., LI, P. & LIU, K. 2010 Large-eddy simulations of the Richtmyer–Meshkov instability of rectangular interfaces accelerated by shock waves. *Sci. Chin. Phys. Mech. Astron.* **53**, 905–914.

YANG, J., KUBOTA, T. & ZUKOSKI, E. E. 1993 Applications of shock-induced mixing to supersonic combustion. *AIAA J.* **31**, 854–862.

YANG, J., KUBOTA, T. & ZUKOSKI, E. E. 1994 A model for characterization of a vortex pair formed by shock passage over a light-gas inhomogeneity. *J. Fluid Mech.* **258**, 217–244.

ZABUSKY, N. J. 1999 Vortex paradigm for accelerated inhomogeneous flows: visiometrics for the Rayleigh–Taylor and Richtmyer–Meshkov environments. *Annu. Rev. Fluid Mech.* **31**, 495–536.

ZHAI, Z., WANG, M., SI, T. & LUO, X. 2014 On the interaction of a planar shock with a light polygonal interface. *J. Fluid Mech.* **757**, 800–816.

ZOU, L., LIU, C., TAN, D., HUANG, W. & LUO, X. 2010 On interaction of shock wave with elliptic gas cylinder. *J. Vis.* **13**, 347–353.

ZUDOV, V. N. 2010 Interaction of shock wave with subsonic heated layer. *Tech. Phys. Lett.* **36** (9), 868–871.

ZUDOV, V. N., TRET'YAKOV, P. K., TUPIKIN, A. V. & YAKOVLEV, V. I. 2003 Supersonic flow past a thermal source. *Fluid Dyn.* **38** (5), 782–793.